INORGANIC CHEMISTRY FRONTIERS

RESEARCH ARTICLE

View Article Online
View Journal

Cite this: DOI: 10.1039/d5qi02586a

Solid-state NMR and theoretical studies illuminate lanthanum borohydride C–H borylation catalysts confined within a zeolite

Jinlei Cui,[a] Yuting Li,[a] Da-Jiang Liu,[a] Marco Mais,[a] Jie Zhang,[a] Long Qi,*[a] Aaron D. Sadow*[a,b] and Takeshi Kobayashi*[a]

Zeolite-supported single-site lanthanum borohydride catalyzes C–H borylation of hydrocarbons, while the related silica-supported complex is inactive under comparable conditions. The identical composition of support-La$(BH_4)_2(THF)_2$ sites in the two materials implies that the support bestows underlying structural features onto La that are required for bond activation catalysis, yet the nature of these effects, which could include confinement effects and/or electronic modulation of the site itself, remains to be identified. We used solid-state nuclear magnetic resonance (SSNMR) spectroscopy and molecular dynamics simulations with machine-learning potentials (ML-MD) to analyze the electronic and steric effects imparted by the faujasite support on the precatalyst structure to correlate with catalytic activity. ML-MD simulations show that THF dissociates from La under the influence of confinement, leading to coordinatively unsaturated sites in the zeolite pores. Then, the La complex grafts on Brønsted acid sites (La^{BAS}) or isolated silanols (La^{SiO}) or remains physisorbed in the zeolite pores. Catalytic studies comparing compounds supported on faujasite zeolites containing or lacking BAS and/or silanols show that only the former complexes lead to active sites, ruling out confinement as the sole requirement for catalysis. The DFT calculations and ML-MD simulations also reveal that the surface-lanthanum coordination number is two (bidentate) for La^{BAS}, with the metal center forming long, flexible bonds to two oxygen atoms bridging Si and Al, but only one oxygen atom (monodentate) for La^{SiO}. The structure–activity relationship identifies confined, BAS-grafted species as active sites and provides important guidance for the design of enhanced atom-efficient catalysts.

Received 23rd December 2025,
Accepted 17th March 2026

DOI: 10.1039/d5qi02586a

rsc.li/frontiers-inorganic

Introduction

Surface organometallic chemistry (SOMC)—the molecular grafting of organometallic complexes onto inorganic oxide surfaces—enables the preparation of well-defined single-site heterogeneous catalysts with similar precision to homogeneous systems.[1–5] Some transformations using SOMC catalysts are faster or show higher selectivity than those using homogeneous analogues, and in some cases the SOMC approach leads to reactions that are otherwise inaccessible. For example, the silica-supported $(\equiv SiO)_3Zr–H$ catalyzes hydrogenolysis of carbon–carbon bonds in hydrocarbons,[6] which is not observed with homogeneous catalysts.[7] Alternatively, SOMC species may be less active than their homogeneous analogues.[8]

Because the metal oxide support acts as a ligand for the SOMC species, the organometallic surface bonding influences activity. For example, zirconium hydride supported on silica–alumina, which also provides surface hydroxyls as grafting sites, is more active for hydrogenolysis.[9] Similarly, WMe_6 supported on silica–alumina is more active in alkane metathesis than the original silica-supported material.[10] Organozirconium supported on acidic sulfated alumina is even more active in alkane hydrogenolysis than silica or silica–alumina supported analogues.[11]

The immobilization of organometallic molecules onto these surfaces also results in a different coordination environment from that of the molecular precursors because of ligand substitution and/or desorption and bond formation with the support. This change in the coordination environment may be one of the reasons why SOMC shows inhibited, enhanced, or new modes of reactivity. Characterization of the coordination geometry of organometallic surface sites, including their interactions with supports, is key to understanding the structures that affect reactivity and to leveraging synthetic control over structure to create more active and more selective catalysts.

Solid-state (SS)NMR spectroscopy, distinguished by its sensitivity to local environments, has become an indispensable tool for probing species at surfaces and interfaces through

[a]U.S. DOE Ames National Laboratory, Iowa State University, Ames, Iowa 50011, USA. E-mail: lqi@ameslab.gov, sadow@iastate.edu, takeshi@iastate.edu
[b]Department of Chemistry, Iowa State University, Ames, Iowa 50011, USA

direct measurement of the metals.[12–15] For example, Gauvin *et al.* analyzed the structure of a scandium amide complex supported on silica using ^{45}Sc NMR, revealing that the amide group is substituted by a ≡SiO– moiety, thereby grafting the complex to the surface, and that the scandium center interacts with neighboring siloxane oxygen atoms.[16] NMR measurements of the central metal in supported organometallic complexes are often limited by low sensitivity due to the low concentration of the complexes and the intrinsically broad NMR spectra of the metal centers. Nevertheless, Copéret *et al.* used dynamic nuclear polarization (DNP)-enhanced SSNMR and high-field NMR to analyze the structure of a molybdenum dioxo complex supported on silica. They found that the structural distortion arising from a sharp ≡SiO–Mo(O)$_2$–OSi≡ bond angle lowers the Mo LUMO, thereby facilitating conversion to an active species.[17] Analysis of supported organometallic complexes is also possible through the SSNMR measurement of organic ligands. For example, Marks *et al.* revealed that HfNp$_4$ (Np = neopentyl) is chemisorbed onto sulfated alumina as HfNp$_2$, and that activation with molecular hydrogen produces Hf(Np)H and HfH$_2$ species that are active for the hydrogenolysis of polyolefins.[11] In the latter approach, quantifying dipolar coupling between nuclei also provides information related to their internuclear distances.[18] These data can be used to establish the coordination geometry of surface species, including the proximity of substituents on ligands to the central metal, to the support surface, and to other ligands. For dynamic species, however, the measurement of internuclear distances can be overestimated by molecular motions that average dipolar interactions.[19] To overcome this complication, the motionally averaged dipolar interactions can be estimated from atomic trajectories predicted by molecular dynamics (MD) simulations,[20] permitting the application of NMR distance measurements to dynamic species.

The acidic sites in crystalline, high surface area zeolites are promising locations for creating highly reactive d^0 or f^{n}d^0 SOMC catalysts, given the trend sulfated alumina > SiO$_2$–Al$_2$O$_3$ > SiO$_2$ in zirconium hydride-catalyzed hydrogenolysis.[11,21] In an example of an organometallic species activated by grafting to a support, rare earth borohydride complexes Ln(BH$_4$)$_3$(THF)$_3$ (Ln = La and Sc) supported on the faujasite zeolite HY$_{30}$ (Si/Al = 30) catalyze the C–H borylation of unactivated hydrocarbons using pinacol borane (HBpin). Similar conditions using the homogeneous molecular precursor complex or silica- or alumina-supported analogues lead to no discernible borylation activity.[22] Furthermore, the yield and turnovers obtained by the HY$_{30}$-supported La catalyst increased 5-fold when the zeolite support reacts with Ph$_3$SiCl, which is larger in dimensions (10.0 × 10.0 × 7.9 Å, Fig. S3) than the HY$_{30}$ micropore aperture (7.4 Å), to exclusively passivate protic sites on the external surface of the zeolite prior to the grafting reaction of La(BH$_4$)$_3$(THF)$_3$. The composition of the grafted complexes, formulated as support-La(BH$_4$)$_2$(THF)$_2$, was determined by elemental analysis, before and after the reaction of the materials with AlMe$_3$, which desorbs THF as THF·AlMe$_3$ as well as BO$_x$H$_y$ species.[23] Intriguingly, the zeolite-supported lanthanum borohydride material manifests a ^{11}B nuclear magnetic resonance (NMR) signal at −16.4 ppm in addition to a signal at −23.1 ppm, which is comparable to the chemical shift of the molecular or silica-supported lanthanum borohydride complexes (–22 ppm). ^{11}B NMR signals in this region are generally attributed to four-coordinated anionic borate species.[24,25] All of these ^{11}B NMR signals are assigned to BH$_4^-$; however, the difference in chemical shifts suggested a distinct coordination and/or electronic environment of the effective precatalyst. The increased intensity of this unique ^{11}B signal in more active materials led to the interpretation that the active species forms *via* reaction of the La complex with ≡Si–O(H)Al≡ (also known as the Brønsted acid sites or BAS). The BAS form at sites where a four-coordinate anionic aluminum substitutes for a four-coordinate framework silicon (≡SiO)$_4$Al–, and a positive charge (*e.g.*, H$^+$ in BAS) satisfies the valence of the fourth oxygen. Because the BAS result from framework silicon substitution, they are located primarily inside the zeolite micropores. Capping the protic sites on the external surface with Ph$_3$Si should increase grafting at the BAS; however, this modification also leads to increased confinement of the lanthanum borohydride species, and this effect could contribute to generating the active species.

A metal-centered SSNMR approach was used to analyze the bonding of scandium borohydride grafted in HY$_{30}$, which also gave an active catalyst for benzene borylation. ^{45}Sc–^{27}Al transfer of population in double-resonance (TRAPDOR) experiments on scandium borohydride-grafted HY$_{30}$ showed that scandium is grafted within 2.7 to 3.1 Å of an aluminum center, *i.e.*, at BAS.[26] In addition, scandium borohydride grafted at BAS (Sc^{BAS}) is monodentate at the ≡SiO(=Al)OSi≡ site and dynamic, hopping back and forth between the two O atoms, whereas species grafted on silica are rigid and form a bidentate Sc–surface coordination *via* one silanoate and one siloxane. As a result, the dynamic Sc^{BAS} in the zeolite pores are more electrophilic than those on silica. This increased electrophilicity could be responsible for the catalytic activity of this zeolite-grafted scandium complex. The grafting reactions at BAS or silanols, the coordination sphere, and the dynamics of lanthanum borohydride, however, could be unique for the largest trivalent lanthanide (1.16 Å 8-coordinate radius) compared to the smallest rare earth Sc (0.87 Å 8-coordinate radius),[27] especially confined in the micropores.

In this study, we established the three-dimensional (3D) structure of the lanthanum borohydride complex grafted at the zeolite BAS (La^{BAS}), employing a combination of SSNMR and theoretical calculations. We further augmented the selective grafting of La precursors (La^{BAS} *vs.* La^{SiO}) by reacting the zeolite support with silanes of different sizes prior to reactions to graft La(BH$_4$)$_3$(THF)$_3$. The correlations between SSNMR signals and the catalytic activity in response to selected silanes further show that La^{BAS} is the precatalyst site, leading to the formation of active species in benzene borylation, while distance measurements reveal distinct coordination chemistry of these sites.

Results and discussion

Solid-state NMR characterization of the zeolite-supported lanthanum borohydride precatalyst

The ^{11}B direct polarization magic-angle spinning (DPMAS) NMR spectrum of the material La$(BH_4)_2(THF)_2$/Ph$_3$Si-HY$_{30}$ (La/Ph$_3$Si-HY$_{30}$), synthesized *via* reaction of La$(BH_4)_3(THF)_3$ and triphenylsilyl-protected HY$_{30}$ (Ph$_3$Si-HY$_{30}$), reveals two distinct signals situated at −16.4 ppm (B1) and −23.1 ppm (B2), as well as a broad signal from −5 to 15 ppm (Fig. 1a). The former two signals are discernible along the chemical shift axis of the 2D ^{11}B multiple quantum (MQ)MAS spectrum (Fig. 1b, diagonal line), indicating distinct magnetic environments of the BH_4-containing species, rather than arising from the second-order perturbed quadrupolar powder pattern. The absence of off-diagonal signals in the 2D ^{11}B–^{11}B SQ/SQ correlation spectrum (Fig. 1c) precludes the possibility that these species reside in the same complex or that there is an exchange between two sites with a correlation time longer than the NMR timescale. The broad signal spanning between −5 ppm and +15 ppm is attributed to BO_xH_y species resulting from the reaction between hydroxy groups and BH_3, generated as a byproduct of La$(BH_4)_3(THF)_3$ grafting. The −16.4 ppm signal (B1) is detected when the complex is grafted onto the aluminosilicate zeolite but not onto silica as La$(BH_4)_2(THF)_2$/SiO$_2$ (La/SiO$_2$; shown as a grey line in Fig. 1a), suggesting that the B1 species is attributed to BH_4 ligands in La^{BAS}. The resonance frequency of the B2 species (−23.1 ppm) closely aligns with that of the BH_4 in La/SiO$_2$ [28] or in La$(BH_4)_3(THF)_3$,[22] suggesting that the B2 signal may arise from multiple species on/in the zeolite, including physisorbed La$(BH_4)_3(THF)_3$ and/or silanol-grafted ≡Si–O–La$(BH_4)_2$.

These assignments are corroborated by ^{11}B{^{27}Al} TRAPDOR[29] experiments, where only the ^{11}B NMR signal of B1 is attenuated by recoupling ^{11}B–^{27}Al dipolar interaction (Fig. 2), demonstrating that the B1 species exclusively resides in close proximity to aluminum. This experiment unambiguously proves that B1 is correctly assigned to BH_4 ligands close to the conjugate base of the BAS. Analysis of the TRAPDOR curve quantified the ^{11}B–^{27}Al dipolar coupling as 100 Hz (Fig. 2). The quantitative determination of the internuclear distance based on this dipolar interaction will be discussed below after considering the dynamics of the surface species.[20]

To investigate the other ^{11}B NMR signals, physisorbed species were generated on purpose by contacting La$(BH_4)_3(THF)_3$ with silane-modified (*via* reaction with Ph$_3$Si-Cl or Me$_3$Si-NMe$_2$) dealuminated zeolite (DA-HY$_{30}$, Si/Al = ∼121) and HY$_{250}$ (Si/Al = 250). Hydroxy site titration reveals that the OH loadings in these zeolite supports are low (Table S2). Tiny signals at 3630 and 3550 cm^{-1} in DRIFTS spectra are associated with BAS, indicating that both HY$_{250}$ and DA-HY$_{30}$ have few BAS (Fig. S2). A small signal at 3595 cm^{-1} in the DRIFTS

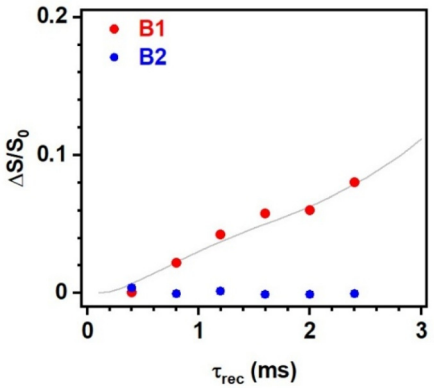

Fig. 2 ^{11}B{^{27}Al} TRAPDOR experiments on La/Ph$_3$Si-HY$_{30}$. The experiments were carried out using a MAS rate of 10 kHz at 110 K, $\nu_{RF}(^{11}B)$ 3 kHz for the initial $\pi/2$ and the inversion π pulses, $\nu_{RF}(^{27}Al)$ = 75 kHz for the heteronuclear recoupling pulse, and $\nu_{RF}(^{1}H)$ = 50 kHz for ^{1}H heteronuclear decoupling. τ_{RD} = 0.8 s and NS = 2400. The grey line represents the best-fit SIMPSON simulated curve with ^{11}B–^{27}Al dipolar coupling of 100 Hz.

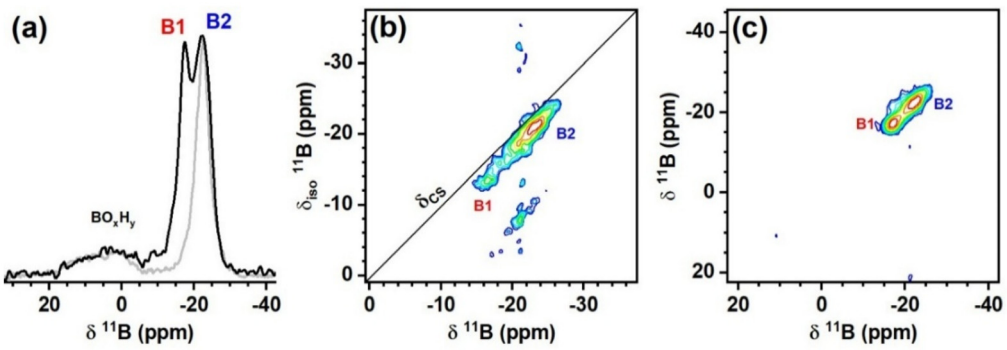

Fig. 1 NMR spectra of La/Ph$_3$Si-HY$_{30}$ and La/SiO$_2$. (a–c) 1D ^{11}B DPMAS, (b) 2D ^{11}B MQMAS, and (c) 2D ^{11}B–^{11}B SQ/SQ correlation spectra of La/Ph$_3$Si-HY$_{30}$, respectively. The grey line in (a) represents the ^{11}B DPMAS NMR spectrum of La/SiO$_2$. The spectra were obtained using ν_R = 5 kHz (a and b) and 10 kHz (c), $\nu_{RF}(^{11}B)$ 6.2 kHz and 100 kHz for soft and hard pulses, and $\nu_{RF}(^{1}H)$ = 50 kHz for ^{1}H heteronuclear decoupling during signal acquisition. The 2D spectra were acquired at 64 t_1 points with Δt_1 = 50 μs and 1440 scans per row (b), and 40 t_1 points with Δt_1 = 100 μs and 800 scans per row (c). Recycle delay τ_{RD} = 0.8 s. The spectra in a and c were recorded at 100 K.

spectrum of DA-HY_{30} is assigned to extra-framework bridging OH,[30,31] resulting from the dealumination process. The modified zeolitic supports Ph_3Si-DA-HY_{30}, Ph_3Si-HY_{250}, and Me_3Si-HY_{250} are also characterized by DNP-enhanced $^{29}Si\{^1H\}$ and $^{13}C\{^1H\}$ CPMAS NMR experiments (Fig. 3a and b). The ^{29}Si NMR signals between −10 ppm and −20 ppm are assigned to organosilyl groups covalently bonded to the zeolite surface. The DNP-enhanced ^{13}C CPMAS spectra (Fig. 3b) confirm the presence of capping agents, and more importantly, their DNP-enhancement ($\varepsilon_{on/off}$), defined as the ratio of signal intensity obtained with and without microwave irradiation, provides insight into the distribution of the capping agent inside and outside the pore. Since the DNP polarizing agent TEKPol is too large to penetrate the zeolite pores, the enhancement of the NMR signal from the internal surface is typically much lower than that observed for the solvent.[32] Therefore, the substantially lower DNP enhancement observed for Me_3Si-HY_{250} ($\varepsilon_{on/off} \sim 12$) compared to that of tetrachloroethene (TCE) solvent ($\varepsilon_{on/off} \sim 80$) indicates that a significant portion of Me_3Si passivated the hydroxy groups within the zeolite pores. In contrast, the comparable DNP enhancements in Ph_3Si-DA-HY_{30} and Ph_3Si-HY_{250} ($\varepsilon_{on/off}$ = 68 and 70, respectively) to that of TCE prove our original assumption that Ph_3Si is predominantly located on the external surface.

The grafting locations of Me_3Si and Ph_3Si are corroborated by IR measurements (Fig. S2a). Approximately 60% of the original intensity of the SiOH peak in the DRIFTS spectrum of DA-HY_{30} (normalized to the framework band at 1860 cm^{-1}) remains in the spectrum of Ph_3Si-DA-HY_{30}, which is consistent with the selective capping of Ph_3SiCl on the external surface of zeolite. In contrast, the SiOH peak decreased by more than 85% in the normalized spectrum of Me_3Si-HY_{250} compared to the signal from HY_{250}. We interpret this difference as evidence that the smaller Me_3SiCl (4.9 × 4.9 × 4.3 Å, Fig. S3), compared to Ph_3SiCl, is able to react with OH groups on the zeolite external surface and within the zeolite pores. Similar external and internal capping was also confirmed by the >65% decrease in intensity of peaks associated with SiOH as well as BAS sites in the normalized spectrum of HY_{30} treated with Me_3SiCl (using the same 1.0 mmol g^{-1} loading as Ph_3SiCl; Fig. S2c). Because not all BAS peaks are quenched in the DRIFTS of this Me_3Si-HY_{30}, the experiment reveals that BAS in certain supercages are still open for grafting with this degree of silylation.

The assignments of La^{SiO} and physisorbed $La(BH_4)_3(THF)_n$ were supported by the ^{11}B DPMAS spectra of the corresponding samples (Fig. 3c). In particular, a prominent signal at −23 ppm appears in the spectrum of La/Ph_3Si-DA-HY_{30}. In this sample, the external surface of the zeolite is capped by Ph_3Si

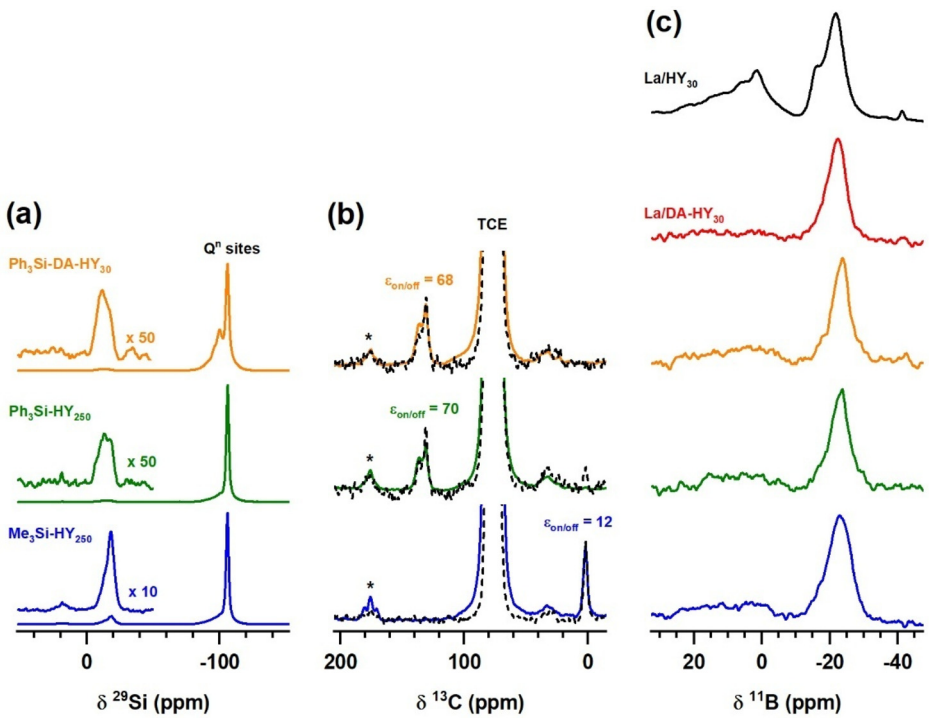

Fig. 3 DNP-enhanced $^{29}Si\{^1H\}$ (a) and $^{13}C\{^1H\}$ CPMAS (b) NMR spectra of zeolitic supports, and ^{11}B DPMAS NMR spectra of lanthanum borohydride-treated modified zeolite (c). The DNP-enhanced spectra were acquired at 110 K using a 16 mM TEKPol solution of 1,1,2,2,-tetrachloroethane, ν_R = 10 kHz, CP contact time = 4 ms (a) and 2 ms (b), $\nu_{RF}(^{29}Si) = \nu_{RF}(^{13}C)$ = 50 kHz during CP, $\nu_{RF}(^1H)$ ramped from 67.5 to 75 kHz during CP and $\nu_{RF}(^1H)$ = 100 kHz during the ^1H hard pulse and SPINAL-64 ^1H decoupling. The recycle delay τ_{RD} = 8.5 s. The dashed black lines in (b) represent the $^{13}C\{^1H\}$ CPMAS spectra recorded without microwave irradiation. Asterisks (*) indicate spinning sidebands of the TCE-d_2 signal. The ^{11}B DPMAS spectra were measured using ν_R = 5 kHz, $\nu_{RF}(^{11}B)$ = 5 kHz during the central-transition selective soft pulse, $\nu_{RF}(^1H)$ = 50 kHz during the two-pulse phase modulated (TPPM) ^1H decoupling, and τ_{RD} = 1.0 s. The spectra were normalized to a constant height for visual clarity.

(as mentioned above), while silanols are formed within the micropores from the hydrolysis of the BAS. From this, La^{SiO} in the BAS-free supercages may be identified by a −23 ppm ^{11}B NMR signal. In La/Me_3Si-HY_{250}, all accessible hydroxy groups are passivated (~0.1 mmol g^{-1}) by reacting excess loading of Me_3Si-NMe_2 with HY_{250} before physisorption of La$(BH_4)_3(THF)_3$. The spectrum of this sample also shows a ^{11}B NMR signal at −23 ppm, indicating that the physisorbed La complex gives rise to the ^{11}B NMR signal at this position. The ^{11}B NMR signals from −5 to 15 ppm, assigned to BH_3-grafted products, are much less intense in silanol- and BAS-free materials. In contrast, the reaction of $Ln(BH_4)_3(THF)_3$ and amorphous silica gives a large signal from −5 to 15 pm.[28] Likely, only a small amount of free BH_3 is generated because $La(BH_4)_3(THF)_3$ barely grafts in these samples, and instead the majority of the −23 ppm signal in both samples comes from physisorbed $La(BH_4)_3(THF)_3$. In addition, the signal at −16.4 ppm diminishes for La/DA-HY_{30}, La/Ph_3Si-DA-HY_{30}, and La/Ph_3Si-HY_{250}, which have low loadings of BAS sites. Thus, this signal is appropriately assigned to La^{BAS}.

Physisorption of lanthanum borohydrides within the zeolite micropores is also illustrated by the comparison of $La(BH_4)_3(THF)_3$ and (coordinated) THF concentrations, measured by solution-phase ^1H NMR spectroscopy, before and after the addition of Me_3Si-SiO_2 (lacking micropores) or Me_3Si-HY_{250} (Fig. S7). The intensity of the ^1H NMR signals assigned to THF and BH_4 is equivalent before and after the addition of nonporous, silylated silica Me_3Si-SiO_2 to the solution, indicating that the $La(BH_4)_3(THF)_3$ complex remains in the liquid phase rather than adsorbing onto the Me_3Si-SiO_2. In contrast, the intensities of the THF and BH_4 signals decrease by 11.8% (~0.0022 mmol) and 16.3% (~0.0030 mmol), respectively, after Me_3Si-HY_{250} (~0.027 g) is added, suggesting that $La(BH_4)_3(THF)_3$ (~0.0010 mmol) is physically trapped in the zeolite pores (and thus invisible to solution NMR measurement). The smaller decrease in the integrated intensity of the THF signals compared to that of the BH_4 corresponds to *ca.* 27% of THF (0.0008 mmol) in $La(BH_4)_3(THF)_3$ (0.0010 mmol), implying that one THF molecule dissociates when $La(BH_4)_3(THF)_3$ enters the micropores.

Structural understanding of the zeolite-supported lanthanum borohydride precatalyst from theory

^{11}B NMR parameters were calculated for surface models of the aforementioned grafted lanthanum borohydride species including La^{BAS}, La^{SiO}, the $La(BH_4)_3(THF)_2$ trapped in the zeolite pores, the $La(BH_4)_3(THF)_3$ precursor, and La/SiO_2. The La^{BAS}, La^{SiO} and physisorbed species were modeled within micropores of a full-size periodic zeolite framework model to accurately replicate a confined environment, rather than being placed on an open surface exposed to free space. Because standard DFT methods typically fail to accurately describe the long-range van der Waals forces originating from dynamic electron correlation, the DFT-D3 Grimme dispersion correlation was included in the calculations.[33,34]

The solvent-exclusion size of the $La(BH_4)_3(THF)_3$ precursor (~11.0 × 8.9 × 7.9 Å) prevents this species from easily diffusing into the ~7.4 Å micropores of HY_{30}. On the other hand, the TRAPDOR experiment on La/Ph_3Si-HY_{30} (Fig. 2) clearly demonstrates that the La complex is in close proximity to Al and thus inside the micropores of the zeolite. To reconcile these two conflicting facts, we considered the possibility that THF dissociates as the precursor enters the pores because it is the least unfavorable ligand to dissociate (Scheme 1) and because THF apparently dissociates upon physisorption (as shown above by an increase in the THF/BH_4 ratio in solution upon the addition of Me_3Si-HY_{250}).

The calculated total electronic energy of $La(BH_4)_3(THF)_2$ and THF in free space is higher by 48 kJ mol^{-1} than La$(BH_4)_3(THF)_3$. Allowing the resulting $La(BH_4)_3(THF)_2$ to infiltrate into the zeolite micropores, however, stabilizes the system by 121 kJ mol^{-1} (*i.e.*, 73 kJ mol^{-1} *vs.* $La(BH_4)_3(THF)_3$). We also evaluated the Gibbs free energy change associated with this series of processes. First, the enthalpy and entropy of La$(BH_4)_3(THF)_3$, $La(BH_4)_3(THF)_2$, and THF at 300 K were determined, from which the Gibbs energy change for THF dissociation (ΔG_1) was estimated to be +24 kJ mol^{-1}. The large size of the model system including the zeolite framework prohibited the calculations of thermal corrections to the calculated adsorption energy. Therefore, the enthalpy change for adsorption of $La(BH_4)_3(THF)_2$ at 300 K was approximated by the total electronic energy change (−121 kJ mol^{-1}), as adsorption is expected to have a negligible effect on the rigid zeolite framework and the difference in thermal contribution between 0 K (for DFT electronic energy calculations) and 300 K should be small. The entropy loss upon adsorption of $La(BH_4)_3(THF)_2$ was estimated to be 267 J mol^{-1} K^{-1} by assuming complete loss of translational and rotational degrees of freedom within the zeolite pores. Given this value, the Gibbs free energy change for adsorption (ΔG_2) was calculated as ΔG_2 = −121 kJ mol^{-1} − 300 K × (−267 J mol^{-1} K^{-1}) = −41 kJ mol^{-1}. Accordingly, the overall Gibbs free energy change for the entire

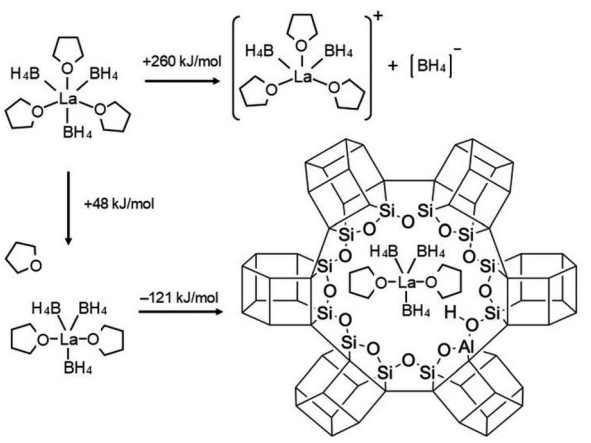

Scheme 1 Ligand dissociation to enable pore adsorption. The energies shown are the total electronic energy.

process was estimated as $\Delta G_1 + \Delta G_2 = -17$ kJ mol^{-1}. Because the translational and rotational motions of $La(BH_4)_3(THF)_2$ are unlikely to be completely quenched upon adsorption in practice, the actual entropy loss is expected to be smaller than this estimate, implying that the process in which $La(BH_4)_3(THF)_3$ releases one THF ligand and diffuses into the zeolite pores is even more thermodynamically favorable.

We attribute the stabilization of the low coordinate lanthanum species to the effect of confinement (Scheme 1). Two key points emerge. First, the confinement effect is critical for lanthanum borohydride to enter and diffuse with the micropores, in terms of its size and geometry. Without confinement stabilizing the smaller $La(BH_4)_3(THF)_2$ intermediate, the lanthanum species would be too large to enter the micropore. Second, confinement creates a thermodynamic driving force for $La(BH_4)_3(THF)_3$ to dissociate THF, enter the micropores, and form a stable, encapsulated structure. Without this effect, the energy penalty of 48 kJ mol^{-1} to dissociate THF would make adsorption of $La(BH_4)_3(THF)_2$ into the pores unfavorable, and diffusion of the La complex into the pores would be driven solely by the chemical potential gradient.

The computed NMR parameters for ^{11}B of {≡SiO(=Al)OSi≡}$La(BH_4)_2(THF)_2$ (Fig. 4a) showed an excellent agreement with those of B1 obtained experimentally (Table 1). In the modeled {κ^2-≡SiO(=Al)OSi≡}$La(BH_4)_2(THF)_2$ low energy structure, the two distances from the La to the oxygen of two Si–O–Al bridges (denoted as O_{BAS}) are equal at approximately 2.7 Å. This distance is longer than the common metal–support distances of 2.1 Å.[35] Thus, immobilization of the La complex by reaction with a BAS results in a bidentate coordination of the surface to La. Notably, optimization of initial structures with monodentate surface-La configurations, in which La is positioned directly above one of the O_{BAS}, also led to the singular bidentate low-energy structure.

The ^{11}B NMR parameters for B2 are also in good agreement with those of models where the La complex is grafted by reaction with silanols, as ≡Si–O–La, either on the zeolite or on an amorphous silica surface (Fig. 4b and d, respectively; Table 1). In the models for both surfaces, the O–La distances are 2.3 Å, while those between the La and the nearest siloxane oxygen were all greater than 4.8 Å, indicating that bonding to silanoate results in monodentate surface-La coordination (*i.e.*, monopodal structures), unlike {κ^2-≡SiO(=Al)OSi≡}$La(BH_4)_2(THF)_2$. In the zeolite model, a lattice defect generates a pair of hydroxy groups. The La grafted to one of the hydroxy groups generated by the lattice defect is 7.9 Å away from the neighboring hydroxy, and the boron atoms of the two BH_4 units are 6.7 Å and 12.3 Å away from the exposed hydroxy group. MD simulations at 300 K, described below, show that the shortest distances between these pairs are 6.6 Å, 6.2 Å, and 10.6 Å, respectively, which are too far to react to create a bipodal $(≡SiO)_2La(BH_4)$ site. The ^{11}B NMR shift of a hypothetical dipodal structure of silanol-grafted lanthanum borohydride species, $(≡SiO–)_2La(BH_4)(THF)_2$, was also calculated. The computed ^{11}B resonance frequency significantly shifted toward the lower frequency side ∼−31 ppm (Fig. S3), and thus this dipodal structure would be precluded. The computed ^{11}B NMR shift for $La(BH_4)_3(THF)_2$ trapped in the zeolite pores, −22.5 ppm, is also in good agreement with that of B2 (Fig. 4c and Table 1), suggesting the presence of physisorbed species.

The long $O_{surface}$–La distances in the faujasite-micropore-confined {κ^2-≡SiO(=Al)OSi≡}$La(BH_4)_2(THF)_2$ and the electron-deficient ≡Si–O–$La(BH_4)_2$ structures illustrated in Fig. 4a and b suggest labile ligand coordination. Therefore, the surface coordination was examined in greater detail using MD simulations with machine-learning (ML) potentials (Fig. 5a). Specifically, ML-MD simulations were performed on the models shown in Fig. 4a and b, with atomic positions recorded every 10 fs over a 1 ns simulation time. During the 1 ns ML-MD simulation at 300 K, the two La–O_{BAS} distances remain nearly equivalent, at around 2.7 Å, indicating that the surface coordination is bidentate, but still fluctuates by ±0.3 Å. The two La–O_{BAS} remain equidistance, but slightly elongated, as the simulation temperature is increased to 500 K (Fig. 5b), indicating that the bidentate structure is maintained. For comparison, the La–$O_{silanol}$ distance in La^{SiO} is shorter than the La–O_{BAS} distance, with smaller fluctuations (2.3 ± 0.2 Å), and these values remain almost unchanged even with increasing

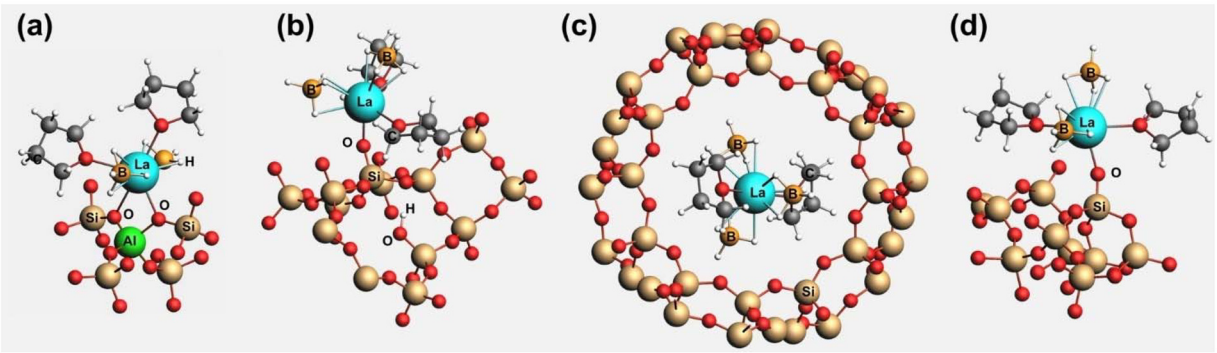

Fig. 4 DFT-optimized structures of La^{BAS} (a), La^{SiO} (b), $La(BH_4)_3(THF)_2$ trapped within the zeolite pores (c), and La/SiO_2 (d). Only the atoms of the framework near lanthanum-zeolite bonds are included in the image. White, grey, red, orange, green, beige, and light blue spheres represent hydrogen, carbon, oxygen, boron, aluminum, silicon, and lanthanum atoms, respectively.

Table 1 Experimentally and theoretically estimated NMR line shape parameters

Species		δ	δ_{iso} (ppm)	C_Q (MHz)	η_Q	P_Q [a] (MHz)	δ_{QIS} [a] (ppm)
B1	Exp.	−16.4	−14.6			1.4	−1.8
La^{BAS} (Fig. 4a)	Calc.	−17.0[b]	−15.4	1.34	0.18	1.35	−1.62
B2	Exp.	−23.1	−21.8			1.2	−1.3
La^{SiO} (Fig. 4b)	Calc.	−22.9[b]	−21.4	1.27	0.20	1.28	−1.46
La, physisorbed (Fig. 4c)	Calc.	−22.5[b]	−21.1	1.25	0.11	1.25	−1.40
La on silica (Fig. 4d)	Calc.	−23.7[b]	−22.7	1.06	0.16	1.06	−1.00
$La(BH_4)_3(THF)_3$ (precursor)	Exp.	−22.2	−20.8			1.49	−1.29
	Calc.	−24.3[b]	−22.9	1.23	0.14	1.23	−1.36

[a] δ_{QIS} (ppm) = $3/17 \times [4S(S+1) - 3]/[4S(2S-1)]^2 \cdot (P_Q^2/\nu_0^2) \times 10^6$, $P_Q \equiv C_Q\sqrt{1+\eta_Q^2/3}$, where S is the spin quantum number of the nucleus, P_Q is the second order quadrupolar effect, ν_0 is the Larmor frequency of the nucleus, C_Q is the quadrupolar coupling constant, and η_Q is the quadrupolar asymmetry parameter. [b] $\delta = \delta_{iso} + \delta_{QIS}$.

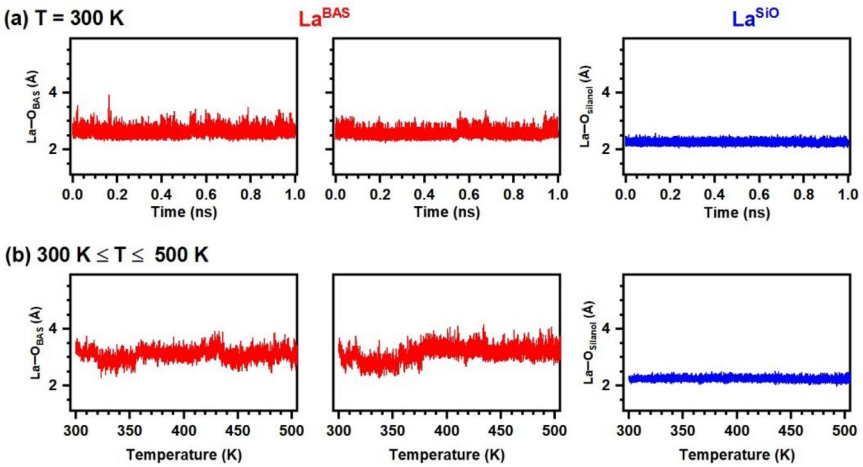

Fig. 5 Internuclear surface oxygen-lanthanum distances in the La^{BAS} and La^{SiO} site models predicted by the ML-MD simulations at 300 K (a) and under temperature ramping from 300 K to 500 K with a 1 K/1 ps rate (b).

temperature. These observations indicate that the La–$O_{silanol}$ bond exhibits a more covalent nature. The determination that La^{BAS} maintains its bidentate configuration contrasts with the structure and dynamics of the lighter Sc congener, which adopts a monodentate configuration and hops between Al-adjacent oxygen sites. Most likely, the smaller size of Sc, which leads to a shorter Ln–O_{Si} distance compared to La, leads to an unfavorable bidentate coordination geometry. These longer La–O distances also reduce steric pressure between the ligands and the pore walls, which, on the other hand, limits Sc–surface coordination. We also note that the number of ligands in the $Sc(BH_4)_3(THF)_2$ precursor is five, whereas six ligands surround $La(BH_4)_3(THF)_3$. While La could reasonably access higher coordination numbers than Sc, bidentate surface coordination in $Sc(BH_4)_2(THF)_2/SiO_2$ compared to monodentate coordination in $Sc(BH_4)_2(THF)_2/Ph_3Si\text{-}HY_{30}$, suggests that the shape of the surface around a grafted metal compound greatly influences the coordination mode.

In contrast to the limited mobility of the La, the ligands exhibited highly dynamic behavior. While the two La···B distances of 2.6 Å remain essentially constant (Fig. 6a), one BH_4 changes its position vigorously relative to the La center (Fig. 6b). Such dynamics likely reduced the ^{11}B–^{27}Al dipolar interaction, making $^{11}B\{^{27}Al\}$ TRAPDOR experiments at room temperature difficult. Rather surprisingly, one THF repeatedly dissociates from and re-coordinates to the La^{BAS} center (Fig. 6a), indicating that one La-bound THF is labilized within the zeolite micropore. An obvious correlation exists between the La–O_{THF} distance and the position of BH_4 relative to the La, suggesting that the dissociation of THF induces the migration of BH_4 in the coordination sphere, or *vice versa*. Furthermore, one THF molecule is also dynamic and labile in the zeolite-confined ≡Si–O–$La(BH_4)_2(THF)_2$ site model (La^{SiO}), ruling out the bidentate surface coordination model at the BAS conjugate base as the cause of THF dissociation. Unstable transients or intermediates from bulky species have been stabilized within the micropores of zeolites by the interaction with the inner surface.[36–38] In the cases of La^{BAS} and La^{SiO}, the confinement effect may have enabled the formation of an undercoordinated state, albeit temporarily.

Significant dynamics were observed for BH_4 also at La^{SiO} (Fig. 6b), but the dissociation of THF is not correlated to the

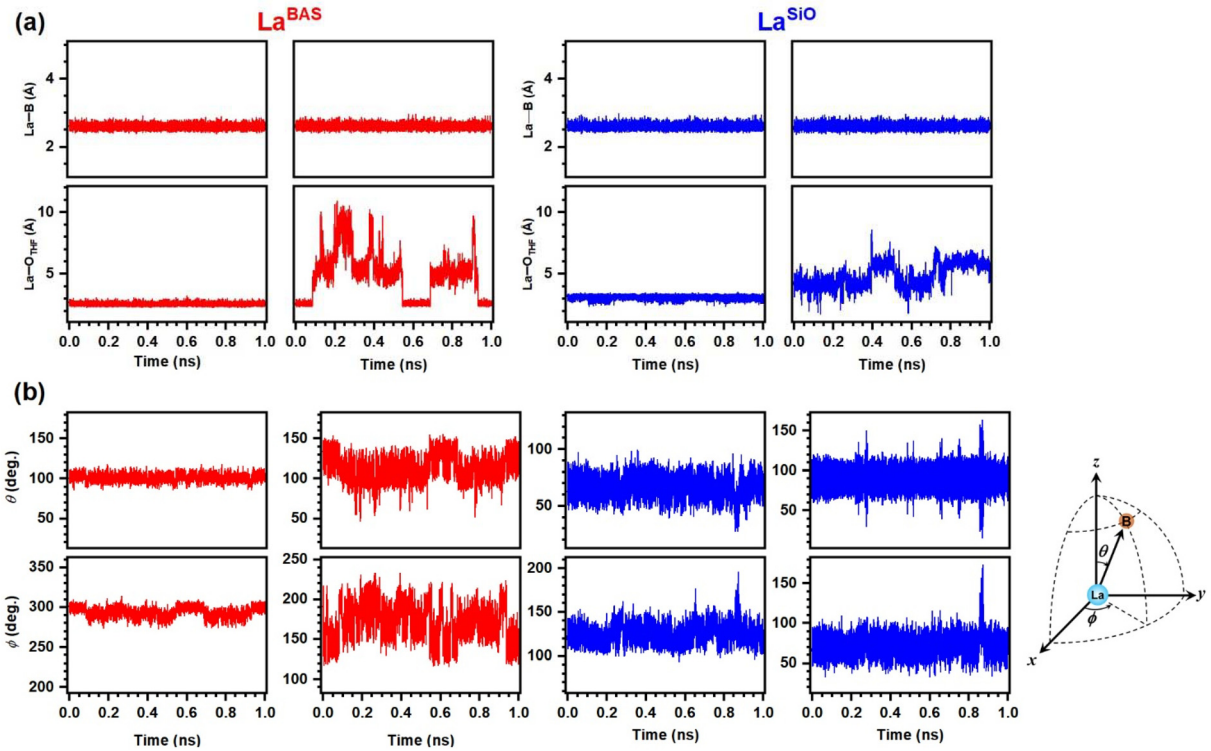

Fig. 6 La–B and La–O_{THF} distances (a) and azimuthal angles θ and polar angle φ representing La → B vectors (b) in the La^{BAS} and La^{SiO} site models predicted by the ML-MD simulations at 300 K.

BH_4 dynamics, unlike the behavior of the La^{BAS}. The BH_4 dynamics at the La^{SiO} may result from its less crowded coordination sphere than at La^{BAS}, from the flexibility of the Si–O–La moiety, or from rotation around the monodentate $O_{surface}$–La bond.

We further scrutinized the consistency between the proposed structure (Fig. 4a) and the TRAPDOR analysis (Fig. 2) using the results of the MD simulations. Dipolar coupling constants are generally inversely proportional to the cube of the internuclear distance.[39] The observable effect of the dipolar interaction additionally depends on the orientation of the internuclear vector with respect to the external magnetic field and is therefore averaged out by molecular motion.[40] Consequently, in dynamic systems such as surface species, relating experimentally observed dipolar coupling to internuclear distances must take into account the time-dependent fluctuations of the internuclear vector. To address this, we calculated the motionally averaged B–Al dipolar coupling by deriving time-dependent internuclear vectors from atomic trajectories obtained *via* MD simulations.[20] At each time step i of the simulation of the La^{BAS} model from Fig. 4a, the Cartesian dipolar coupling tensor in the laboratory frame, $\boldsymbol{D}_{LAB}$, was computed based on the internuclear vector (Fig. 7a), and a rolling average of the tensor

$$\boldsymbol{D} = \frac{1}{N}\sum_{i=1}^{N} \boldsymbol{D}_{LAB,i}$$

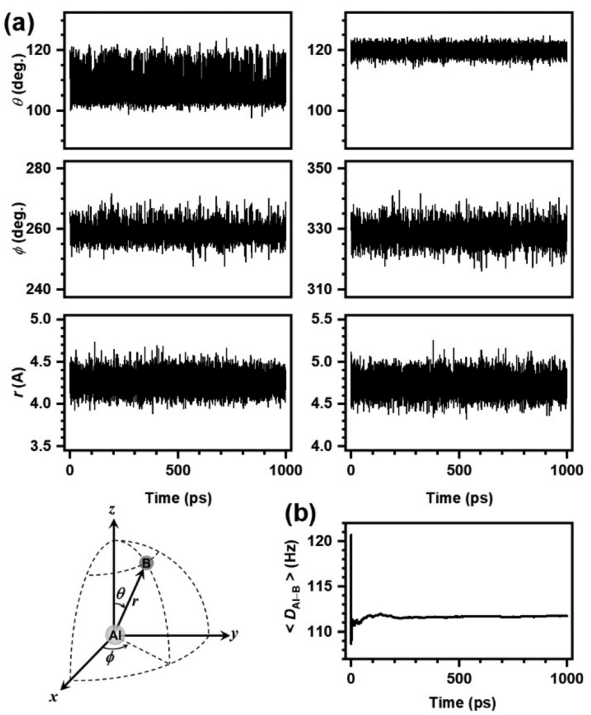

Fig. 7 Azimuthal angle θ and polar angle ϕ, and B–Al distances (a) and the evaluation of B–Al dipolar coupling (b) as a function of the MD simulation time. The dipolar coupling represents the average of two B–Al pairs.

was calculated. Diagonalization of $\langle \boldsymbol{D} \rangle$ yielded the motionally averaged dipolar coupling constant $\langle \boldsymbol{D} \rangle$. By plotting $\langle \boldsymbol{D} \rangle$ as a function of the simulation time, we access its convergence and its steady-state values (Fig. 7b).[20] The estimated motionally averaged dipolar coupling and the B–Al internuclear distance are 112 Hz and 4.5 Å, respectively, which are in reasonable agreement with the values of 100 Hz and 4.6 Å from the TRAPDOR experiment. The small motional averaging of the dipolar interaction is most likely attributed to the slight displacement of the La relative to the surface, the suppression of ligand dynamics at lower temperatures, and the inherently small angular fluctuation of the internuclear vector resulting from the long interatomic distance.

Catalytic activity of zeolite-supported lanthanum borohydrides

We then sought to identify which of the surface species identified above are precatalyst sites for benzene borylation. As extensively established by SSNMR and ML-MD simulations above, potential sites include BAS or silanol grafted species that are confined in supercages of the zeolite micropores or on external or mesopore-exposed surfaces. Here, we again note that our previous studies revealed that blocking Ln reactions on the outer surface of the zeolite led to increased activity and implied that immobilization inside pores was responsible. The activity of the sites themselves could result from confinement and/or grafting at BAS, and both of these factors were affected by our previous protocol and both influence lanthanum borohydride coordination chemistry. To distinguish these effects, lanthanum borohydride was grafted on faujasite supports containing BAS and external and internal silanols (La/HY_{30}), low, medium and high loadings of Al/BAS and internal silanols (La/Ph_3Si-HY_{15}, La/Ph_3Si-HY_{30}, and La/Ph_3Si-HY_{50}), external and internal silanols (La/DA-HY_{30}), only internal silanols (La/Ph_3Si-DA-HY_{30}), and grafting-site free (La/Me_3Si-HY_{250}, *i.e.*, physisorbed La) and these materials were heated in benzene with HBpin under the reaction conditions given in Table 2.

Our previous studies[22,23] showed a higher yield of PhBpin from La/Ph_3Si-HY_{30} (7.6%) compared to La/HY_{30} (1.6%), corresponding to a 5-fold increase in turnovers. Grafting $La(BH_4)_3(THF)_3$ on Ph_3Si-HY_{30} resulted in a slightly lower La loading (0.07 $mmol_{La}$ g^{-1}) in La/Ph_3Si-HY_{30} compared to 0.09 $mmol_{La}$ g^{-1} in La/HY_{30}. The capping of the external surface of HY_{30} (0.86 mmol OH per g) with Ph_3SiCl consumed *ca.* 0.4 mmol OH per g, leaving 0.46 mmol OH per g. Furthermore, the hydroxy species on the external surface are primarily silanols. Thus, the ~50% decrease in OH upon external capping compared to only a ~20% decrease in lanthanum loading suggested a higher ratio of lanthanum borohydride sites grafted inside the micropores to form La^{BAS} sites in La/Ph_3Si-HY_{30} compared to La/HY_{30}. We previously interpreted these results to indicate that the lanthanum grafted at BAS, now structurally characterized as La^{BAS}, leads to active sites for benzene borylation.

In addition to more La^{BAS} correlating with higher activity, there is an additional effect of Ph_3SiCl capping on the catalysis. There are fewer accessible uncapped BAS in La/Ph_3Si-HY_{30} compared to La/HY_{30} because more BAS are converted into La^{BAS}. HBpin decomposition is catalyzed by free BAS. Thus, the BAS-catalyzed side reaction is slower in La/Ph_3Si-HY_{30} than La/HY_{30}. Both effects lead to higher yields and higher selectivity in the capped catalyst. In this context, we point out that activity and selectivity for PhBpin depend on the HBpin conversion rate *vs.* the PhBpin formation rate.

In this context, we investigated BAS loading on catalysis by grafting $La(BH_4)_3(THF)_3$ on Ph_3Si-capped HY zeolites with high (Si/Al = 15 in La/Ph_3Si-HY_{15}) or low (Si/Al = 50 in La/Ph_3Si-HY_{50}) aluminum content. The trend in Al content in HY_{15}, HY_{30}, and HY_{50} parallels the non-quantitative relative intensity of the framework-normalized BAS signals in DRIFTS (Fig. S2e and S2f). The trend in HBpin conversion is La/Ph_3Si-HY_{15} (0.20 M h^{-1}) > La/Ph_3Si-HY_{30} (0.16 M h^{-1}) > La/Ph_3Si-HY_{50} (0.03 M h^{-1}). We attribute the faster HBpin conversion to higher BAS and higher La^{BAS}. In contrast, the selectivity for PhBpin is high for La/Ph_3Si-HY_{50} (8.1%) and low for La/Ph_3Si-HY_{15} (2.1%). As a result, the yield of PhBpin was lower in these samples than in La/Ph_3Si-HY_{15}. BAS provides a site for

Table 2 C–H borylation of benzene catalyzed by the lanthanum borohydride complex grafted on different supports[a]

	La loading (mmol g^{-1})	HBpin Conversion (%)	PhBpin Yield (%)	PhBpin Turnovers	PhBpin Selectivity (%)	Initial rate constant	
						HBpin conversion (M h^{-1})	PhBpin formation (mM h^{-1})
La/HY_{30}	0.09	99	1.6	10	1.8	0.27	7.6
La/Ph_3Si-HY_{30}	0.07	95	7.6	45	7.9	0.16	9.4
La/Ph_3Si-HY_{15}	0.10	99	2.1	8	2.1	0.20	4.1
La/Ph_3Si-HY_{50}	0.06	12	0.97	6	8.1	0.03	1.2
La/Ph_2MeSi-HY_{30}	0.06	98	6.0	42	6.1	0.15	7.9
La/Me_3Si-HY_{30}	0.07	77	4.4	26	5.7	0.08	5.2
La/SiO_2	0.12	<1	~0	n.a.[b]	n.a.[b]	n.a.[b]	n.a.[b]
La/DA-HY_{30}	0.10	4.3	~0	n.a.[b]	n.a.[b]	n.a.[b]	n.a.[b]
La/Ph_3Si-DA-HY_{30}	0.07	3.7	~0	n.a.[b]	n.a.[b]	n.a.[b]	n.a.[b]
La/Ph_3Si-HY_{250}	0.08	5.4	~0	n.a.[b]	n.a.[b]	n.a.[b]	n.a.[b]
La/Me_3Si-HY_{250}	0.03	2.2	~0	n.a.[b]	n.a.[b]	n.a.[b]	n.a.[b]

[a] Conditions: 0.025 g precatalysts, 0.5 mL benzene, 0.15 mL HBpin (~1.0 mmol), 120 °C, 12 h. [b] Not applicable.

forming active species while at the same time causing the degradation of HBpin,[23] and thus, a monotonic correlation was not observed between the Si/Al ratio and the PhBpin yield.

We also tested different sized capping agents at similar loading to establish the external grafting of Ph_3Si compared to smaller silyl groups. The idea that Ph_3SiCl, primarily grafted on the external surface of HY_{30}, should affect catalysis differently from other silane capping locations was tested by reaction with the slightly smaller chlorosilane $Ph_2MeSiCl$ or the much smaller Me_3SiCl, at similar loadings as in Ph_3Si-HY_{30} (and in contrast to experiments of Me_3Si-HY_{250}, where Me_3SiCl capped all accessible OHs). The size of $Ph_2MeSiCl$ (9.5 × 7.9 × 4.6 Å, Fig. S3) approaches that of the pore diameter, while Me_3SiCl is smaller than the pore diameter as noted above. Similar OH loadings in Ph_2MeSi-HY_{30} and Me_3Si-HY_{30} of 0.42 and 0.39 mmol g^{-1}, respectively, indicate a similar degree of capping. The La loadings in the catalyst samples La/Ph_2MeSi-HY_{30} (0.06 mmol La per g) and La/Me_3Si-HY_{30} (0.07 mmol g^{-1}) were also similar to La/Ph_3Si-HY_{30}. ^{11}B SSNMR spectra of these materials all include the B1 signal (Fig. S4) assigned to La^{BAS}. The catalytic activities of La/Ph_2MeSi-HY_{30} (42 turnovers) and La/Ph_3Si-HY_{30} (45 turnovers) were comparable. These experiments support the idea that SiOH defects on the external surface and in mesopores of HY_{30} are effectively capped by Ph_3SiCl since the smaller $Ph_2MeSiCl$ appears to graft similarly. La/Me_3Si-HY_{30}, in contrast, gave only 26 turnovers. Since Me_3SiCl can cap both BAS in micropores and silanols on the external surface, lower HBpin conversion and fewer turnovers for PhBpin formation indicate that fewer BAS are accessible to HBpin and a smaller fraction of La sites are active.

The silanol-rich and BAS-poor zeolite DA-HY_{30} was studied to probe the C–H borylation activity of silanol-grafted La sites on and confined within the zeolite. ^{11}B SSNMR spectra of La/DA-HY_{30} and its externally silylated derivative, La/Ph_3Si-DA-HY_{30}, did not contain detectable signals at −16.4 ppm. A catalytic test of this material produced HBpin, with <5% conversion; PhBpin was not detected in the reaction mixture by ^{11}B NMR or GC-MS. This material shows that silanol-grafted $\equiv$SiO–$La(BH_4)_2(THF)_n$ species, inside and outside micropores of the zeolite, are not catalytically active for benzene borylation or HBpin decomposition under these conditions.

The selective external silylation of DA-HY_{30}, to favor micropore- and silanol-grafted lanthanum species, also decreased the La loading from 0.10 $mmol_{La}$ g^{-1} in La/DA-HY_{30} to 0.07 $mmol_{La}$ g^{-1} in La/Ph_3Si-DA-HY_{30}. Unlike the La/Ph_3Si-HY_{30}-improved PhBpin yield compared to La/HY_{30}, La/Ph_3Si-DA-HY_{30} also gave <5% HBpin conversion and PhBpin was not detected. Thus, confined, silanol-grafted lanthanum borohydride is also insufficient to generate active sites. For the same reasons, 0.08 $mmol_{La}$ g^{-1} La/Ph_3Si-HY_{250} is catalytically inactive under these conditions, giving <5% HBpin decomposition. Capping HY_{250} with Me_3SiCl further reduced accessible silanols and BAS for grafting. The La loading in La/Me_3Si-HY_{250} was only 0.03 $mmol_{La}$ g^{-1}, with La mostly in the form of physisorbed species inside the faujasite micropores, and catalytic activity was not observed. These results indicate that confinement of $O_{surface}$–$La(BH_4)_2(THF)_2$ or even physisorbed $La(BH_4)_3(THF)_2$ is not sufficient to generate active sites, and La^{BAS} is an essential species for C–H borylation under these conditions.

Conclusion

This study reveals that confinement effects and surface coordination act synergistically to create uniquely active La^{BAS} for benzene borylation. First, confinement generates the thermodynamic and geometric conditions required for lanthanum borohydride to enter the micropores of the faujasite zeolite. Without confinement to create the driving force for THF to dissociate from $La(BH_4)_3(THF)_3$, coupled to the formation of an appropriately sized $La(BH_4)_3(THF)_2$ intermediate, lanthanum borohydride could not physisorb into the micropores and graft on internal silanols or BAS. Second, lanthanum coordinates to the conjugate base of BAS and to surface silanoates *via* bidentate or monodentate modes, respectively.

We demonstrated that the confined silanoate-coordinated La^{SiO} species are inactive in benzene borylation, even though their coordination number is lower than the bidentate surface-coordinated La^{BAS} species. This surface coordination mode is important to form the active catalyst, but not essential, since the smaller Sc center bonds to BAS in a monodentate fashion and also leads to catalytically active species. In fact, scandium forms an inactive, bidentate surface coordinated species on silica. On the other hand, the O–La distance of 2.7 Å in La^{BAS} determined by a combination of SSNMR and ML-MD simulations is longer than the 2.3 Å O–La distance in La^{SiO}. That is, the weak surface coordination in La^{BAS} leads to an undercoordinated species and is likely a significant contributor to its reactivity. The high catalytic activity associated with these sites also correlates with the dynamic coordination of THF to lanthanum under pore confinement.

Experimental

Catalyst preparation

Lanthanum borohydrides grafted on supports. The grafting of lanthanum borohydrides on surface-modified faujasite supports or silica was conducted according to the reported method.[22] The lanthanum borohydride complex $La(BH_4)_3(THF)_3$ (0.040 g, 0.10 mmol) was dissolved in toluene (5 mL) at room temperature, and the resulting solution was added to the support material (*e.g.*, 0.350 g of Ph_3Si-HY_{30}). The reaction mixture was stirred for 20 h at room temperature to graft $La(BH_4)_3(THF)_3$ onto each support material, including HY_{30}, Ph_3Si-HY_{30}, dealuminated HY_{30} (DA-HY_{30}), Ph_3Si-DA-HY_{30}, Ph_3Si-HY_{250}, Me_3Si-HY_{30} and SiO_2. The precatalysts are herein denoted as La/supports, for example, La/Ph_3Si-HY_{30}. Further details for the material synthesis and analyses, catalyst testing, and product analysis are given in the Supplemental Information.

Structural characterization

Solid-state NMR. Solid-state NMR experiments were conducted at 9.4 T, on an Agilent DDR2 spectrometer, equipped with a Chemagnetics 5 mm double resonance magic-angle spinning (MAS) probe (one-dimensional (1D) ^{11}B direct polarization (DP) MAS and two-dimensional (2D) ^{11}B multi-quantum (MQ)MAS NMR experiments), and a Bruker Biospin DNP-SSNMR spectrometer equipped with a 3.2 mm low-temperature triple-resonance MAS probe (1D ^{29}Si{^{1}H}, ^{13}C{^{1}H} DNP-enhanced CPMAS, ^{11}B{^{27}Al} TRAPDOR and 2D ^{11}B single-quantum/single quantum (SQ/SQ) correlation NMR experiments). For DNP-enhanced ^{29}Si{^{1}H} and ^{13}C{^{1}H} CPMAS experiments, silylated samples were impregnated with a 16 mM solution of TEKPol in 1,1,2,2-tetrachloroethane (TCE). The samples were packed in a high-temperature/high-pressure 5 mm zirconia rotor (Revolution NMR) or 3.2 mm sapphire rotors (Bruker) in an argon glovebox and spun using dry nitrogen gas to avoid decomposition of the La complex due to ambient moisture.

NMR parameter calculations. Surface models were created using the zeolite and silica models adopted from the previous reports.[41,42] Specifically, the zeolite model is periodic and infinitely extended based on the unit cell. A BAS was introduced by substituting one Si atom at the entrance of the supercage – the most accessible location – with Al (one Al per supercage). The silanolate site within the zeolite pore was created by cleaving the siloxane bridge at the same position. For these models, density functional theory (DFT) calculations of structures and NMR parameters were conducted, employing the Quantum Espresso package, version 7.1.[43,44] The structural optimization was performed using the generalized gradient approximation (GGA) of Perdew, Burke and Ernzerhof (PBE) as the exchange–correlation functional.[45] Depending on the element, either ultra-soft pseudopotentials or projector augmented wave (PAW) potentials, available at the materials cloud website,[46] were used. All atoms, including those in the zeolite framework, were subjected to structural optimization. For the structure-refined models, the NMR shielding tensors were computed using the gauge-including PAW (GIPAW) method[47] with the GIPAW pseudopotentials developed by Ceresoli *et al.*[48] Kinetic energy cutoffs of 40 Ry (544 eV) and 80 Ry (1088 eV) were used for structural optimization and NMR calculations, respectively, and a 2 × 2 × 2 Monkhorst–Pack grid[49] was used for k-space sampling in all calculations.

Molecular dynamics (MD) simulations. MD simulations of models of the zeolite- or silica-supported lanthanum borohydride complex were performed at 300 K for a duration of 1 ns. Interatomic interactions were modeled by a machine learning (ML) potential derived from DFT calculations using the PBE functional.[45] DFT calculations are carried out using the VASP code,[50,51] and the Deep Potential for Molecular Dynamics (DeePMD) framework and codes[52] were employed for the training of the ML potential. The basic methodology is given in ref. 53. Additional optimization necessitated by the large number (7) of elements was undertaken, with details provided in the SI. Simulations were performed using an amount, volume, and temperature (NVT) ensemble with Langevin dynamics, utilizing the built-in MD tools in Atomic Simulation Environment (ASE).[54] The time step was 0.5 fs, with a 0.002 friction term to maintain the desired temperature.

Conflicts of interest

There are no conflicts to declare.

Data availability

The data that support the findings of this study are available at Datashare, an open-access repository at Iowa State University at **https://doi.org/10.25380/iastate.31258684**.

Supplementary information (SI) is available. See DOI: **https://doi.org/10.1039/d5qi02586a**.

Acknowledgements

This research was supported by the U.S. Department of Energy, Office of Science, Office of Basic Energy Sciences, Chemical Sciences, Geosciences, and Biosciences Division, Catalysis Science program. MD simulations (D.-J. Liu) were supported under the Computational and Theoretical (CTC) project. Ames National Laboratory is operated for the U.S. Department of Energy by Iowa State University under Contract No. DEAC02-07CH11358.

References

1 M. K. Samantaray, V. D'Elia, E. Pump, L. Falivene, M. Harb, S. O. Chikh, L. Cavallo and J.-M. Basset, The Comparison between Single Atom Catalysis and Surface Organometallic Catalysis, *Chem. Rev.*, 2020, **120**, 734–813.

2 M. K. Samantaray, E. Pump, A. Bendjeriou-Sedjerari, V. D'Elia, J. D. A. Pelletier, M. Guidotti, R. Psaro and J.-M. Basset, Surface Organometallic Chemistry in Heterogeneous Catalysis, *Chem. Soc. Rev.*, 2018, **47**, 8403–8437.

3 C. Copéret, A. Comas-Vives, M. P. Conley, D. P. Estes, A. Fedorov, V. Mougel, H. Nagae, F. Núñez-Zarur and P. A. Zhizhko, Surface Organometallic and Coordination Chemistry toward Single-Site Heterogeneous Catalysts: Strategies, Methods, Structures, and Activities, *Chem. Rev.*, 2016, **116**, 323–421.

4 C. Copéret, M. Chabanas, R. P. Saint-Arroman and J.-M. Basset, Homogeneous and Heterogeneous Catalysis: Bridging the Gap through Surface Organometallic Chemistry, *Angew. Chem., Int. Ed.*, 2003, **42**, 156–181.

5 B. C. Gates, Mononuclear Metal Complex Catalysts on Supports: Foundations in Organometallic and Surface

Chemistry and Insights into Structure, Reactivity, and Catalysis, *Chem. Sci.*, 2024, **15**, 16821–16843.

6 C. Lecuyer, F. Quignard, A. Choplin, D. Olivier and J. M. Basset, Surface Organometallic Chemistry on Oxides - Selective Catalytic Low-Temperature Hydrogenolysis of Alkanes by a Highly Electrophilic Zirconium Hydride Complex Supported on Silica, *Angew. Chem., Int. Ed.*, 1991, **30**, 1660–1661.

7 J. Corker, F. Lefebvre, C. Lecuyer, V. Dufaud, F. Quignard, A. Choplin, J. Evans and J. M. Basset, Catalytic Cleavage of the C-H and C-C Bonds of Alkanes by Surface Organometallic Chemistry: An Exafs and Ir Characterization of a Zr-H Catalyst, *Science*, 1996, **271**, 966–969.

8 N. Eedugurala, Z. Wang, K. Yan, K. C. Boteju, U. Chaudhary, T. Kobayashi, A. Ellern, I. I. Slowing, M. Pruski and A. D. Sadow, B-Sih-Containing Tris(Silazido) Rare-Earth Complexes as Homogeneous and Grafted Single-Site Catalyst Precursors for Hydroamination, *Organometallics*, 2017, **36**, 1142–1153.

9 V. Dufaud and J.-M. Basset, Catalytic Hydrogenolysis at Low Temperature and Pressure of Polyethylene and Polypropylene to Diesels or Lower Alkanes by a Zirconium Hydride Supported on Silica-Alumina: A Step toward Polyolefin Degradation by the Microscopic Reverse of Ziegler–Natta Polymerization, *Angew. Chem., Int. Ed.*, 1998, **37**, 806–810.

10 M. K. Samantaray, R. Dey, E. Abou-Hamad, A. Hamieh and J.-M. Basset, Effect of Support on Metathesis of *n*-Decane: Drastic Improvement in Alkane Metathesis with WMe_5 Linked to Silica–Alumina, *Chem. – Eur. J.*, 2015, **21**, 6100–6106.

11 W. C. Edenfield, A. H. Mason, Q. H. Lai, A. Agarwal, T. Kobayashi, Y. Kratish and T. J. Marks, Rapid Polyolefin Plastic Hydrogenolysis Mediated by Single-Site Heterogeneous Electrophilic/Cationic Organo-Group Iv Catalysts, *ACS Catal.*, 2023, **14**, 554–565.

12 R. Lang, X. Du, Y. Huang, X. Jiang, Q. Zhang, Y. Guo, K. Liu, B. Qiao, A. Wang and T. Zhang, Single-Atom Catalysts Based on the Metal–Oxide Interaction, *Chem. Rev.*, 2020, **120**, 11986–12043.

13 J. Li, M. F. Stephanopoulos and Y. Xia, Introduction: Heterogeneous Single-Atom Catalysis, *Chem. Rev.*, 2020, **120**, 11699–11702.

14 S. K. Kaiser, Z. Chen, D. F. Akl, S. Mitchell and J. Pérez-Ramírez, Single-Atom Catalysts across the Periodic Table, *Chem. Rev.*, 2020, **120**, 11703–11809.

15 A. Q. Wang, J. Li and T. Zhang, Heterogeneous Single-Atom Catalysis, *Nat. Rev. Chem.*, 2018, **2**, 65–81.

16 T. Vancompernolle, X. Trivelli, L. Delevoye, F. Pourpoint and R. M. Gauvin, On the Use of Solid-State ^{45}Sc NMR for Structural Investigations of Molecular and Silica-Supported Scandium Amide Catalysts, *Dalton Trans.*, 2017, **46**, 13176–13179.

17 Z. J. Berkson, R. Zhu, C. Ehinger, L. Lätsch, S. P. Schmid, D. Nater, S. Pollitt, O. V. Safonova, S. Björgvinsdóttir, A. B. Barnes, *et al.*, Active Site Descriptors from ^{95}Mo NMR Signatures of Silica-Supported Mo-Based Olefin Metathesis Catalysts, *J. Am. Chem. Soc.*, 2023, **145**, 12651–12662.

18 R. Jabbour, M. Renom-Carrasco, K. W. Chan, L. Völker, P. Berruyer, Z. R. Wang, C. M. Widdifield, M. Lelli, D. Gajan, C. Copéret, *et al.*, Multiple Surface Site Three-Dimensional Structure Determination of a Supported Molecular Catalyst, *J. Am. Chem. Soc.*, 2022, **144**, 10270–10281.

19 Y. Ishii, T. Terao and S. Hayashi, Theory and Simulation of Vibrational Effects on Structural Measurements by Solid-State Nuclear Magnetic Resonance, *J. Chem. Phys.*, 1997, **107**, 2760–2774.

20 T. Kobayashi, D. J. Liu and F. A. Perras, Spatial Arrangement of Dynamic Surface Species from Solid-State NMR and Machine Learning-Accelerated MD Simulations, *Chem. Commun.*, 2022, **58**, 13939–13942.

21 V. R. Dufaud and J. M. Basset, Catalytic Hydrogenolysis at Low Temperature and Pressure of Polyethylene and Polypropylene to Diesels or Lower Alkanes by a Zirconium Hydride Supported on Silica-Alumina: A Step toward Polyolefin Degradation by the Microscopic Reverse of Ziegler-Natta Polymerization, *Angew. Chem., Int. Ed.*, 1998, **37**, 806–810.

22 Y. Li, U. Kanbur, J. Cui, G. Wang, T. Kobayashi, A. D. Sadow and L. Qi, Supported Lanthanum Borohydride Catalyzes CH Borylation inside Zeolite Micropores, *Angew. Chem., Int. Ed.*, 2022, **61**, e202117394.

23 Y. Li, T. Kobayashi, D. M. Meira, L. An, L. Qi and A. D. Sadow, Trimethylaluminum Activates Zeolite-Confined Lanthanum Borohydrides to Enhance Catalytic C–H Borylation, *J. Am. Chem. Soc.*, 2025, **147**, 12574–12586.

24 Z. Lodziana, P. Blonski, Y. G. Yan, D. Rentsch and A. Remhof, NMR Chemical Shifts of ^{11}B in Metal Borohydrides from First-Principle Calculations, *J. Phys. Chem. C*, 2014, **118**, 6594–6603.

25 S. Hermanek, B-11 NMR-Spectra of Boranes, Main-Group Heteroboranes, and Substituted Derivatives - Factors Influencing Chemical-Shifts of Skeletal Atoms, *Chem. Rev.*, 1992, **92**, 325–362.

26 S. A. Southern, Y. Li, D.-J. Liu, A. D. Sadow, L. Qi and F. A. Perras, Enhanced Activity from Coordinatively Unsaturated and Dynamic Zeolite-Bound Organoscandium Species, *ACS Catal.*, 2024, **14**, 9440–9451.

27 R. D. Shannon, Revised Effective Ionic-Radii and Systematic Studies of Interatomic Distances in Halides and Chalcogenides, *Acta Crystallogr., Sect. A*, 1976, **32**, 751–767.

28 N. Ajellal, G. Durieux, L. Delevoye, G. Tricot, C. Dujardin, C. M. Thomas and R. M. Gauvin, Polymerization of Racemic B-Butyrolactone Using Supported Catalysts: A Simple Access to Isotactic Polymers, *Chem. Commun.*, 2010, **46**, 1032–1034.

29 E. R. H. Vaneck, R. Janssen, W. Maas and W. S. Veeman, A Novel Application of Nuclear Spin-Echo Double-Resonance to Aluminophosphates and Aluminosilicates, *Chem. Phys. Lett.*, 1990, **174**, 428–432.

30 S. M. T. Almutairi, B. Mezari, G. A. Filonenko, P. Magusin, M. S. Rigutto, E. A. Pidko and E. J. M. Hensen, Influence of Extraframework Aluminum on the Bronsted Acidity and Catalytic Reactivity of Faujasite Zeolite, *ChemCatChem*, 2013, **5**, 452–466.
31 T. W. Beutel, A. M. Willard, C. Lee, M. S. Martinez and R. Dugan, Probing External Bronsted Acid Sites in Large Pore Zeolites with Infrared Spectroscopy of Adsorbed 2,4,6-Tri-Tert-Butylpyridine, *J. Phys. Chem. C*, 2021, **125**, 8518–8532.
32 L. Lakiss, C. Kouvatas, J. P. Gilson, V. Valtchev, S. Mintova, C. Fernandez, R. Bedard, S. Abdo and J. Bricker, Atomic-Insight into Zeolite Catalyst Forming-an Advanced NMR Study, *J. Phys. Chem. C*, 2021, **125**, 20028–20034.
33 S. Grimme, J. Antony, S. Ehrlich and H. Krieg, A Consistent and Accurate Ab Initio Parametrization of Density Functional Dispersion Correction (DFT-D) for the 94 Elements H-Pu, *J. Chem. Phys.*, 2010, **132**, 154104.
34 S. Grimme, S. Ehrlich and L. Goerigk, Effect of the Damping Function in Dispersion Corrected Density Functional Theory, *J. Comput. Chem.*, 2011, **32**, 1456–1465.
35 O. Alexeev and B. C. Gates, EXAFS Characterization of Supported Metal-Complex and Metal-Cluster Catalysts Made from Organometallic Precursors, *Top. Catal.*, 2000, **10**, 273–293.
36 E. G. Derouane, Zeolites as Solid Solvents, *J. Mol. Catal. A: Chem.*, 1998, **134**, 29–45.
37 G. Noh, Z. C. Shi, S. I. Zones and E. Iglesia, Isomerization and B-Scission Reactions of Alkanes on Bifunctional Metal Acid Catalysts: Consequences of Confinement and Diffusional Constraints on Reactivity and Selectivity, *J. Catal.*, 2018, **368**, 389–410.
38 S. P. Crossley, D. E. Resasco and G. L. Haller, Clarifying the Multiple Roles of Confinement in Zeolites: From Stabilization of Transition States to Modification of Internal Diffusion Rates, *J. Catal.*, 2019, **372**, 382–387.
39 M. Ernst, S. Bush, A. C. Kolbert and A. Pines, Second-Order Recoupling of Chemical-Shielding and Dipolar-Coupling Tensors under Spin Decoupling in Solid-State NMR, *J. Chem. Phys.*, 1996, **105**, 3387–3397.
40 P. Schanda, M. Huber, J. Boisbouvier, B. H. Meier and M. Ernst, Solid-State NMR Measurements of Asymmetric Dipolar Couplings Provide Insight into Protein Side-Chain Motion, *Angew. Chem., Int. Ed.*, 2011, **50**, 11005–11009.
41 J. N. Louwen, S. Simko, K. Stanciakova, R. E. Bulo, B. M. Weckhuysen and E. T. C. Vogt, Role of Rare Earth Ions in the Prevention of Dealumination of Zeolite Y for Fluid Cracking Catalysts, *J. Phys. Chem. C*, 2020, **124**, 4626–4636.
42 A. Comas-Vives, Amorphous SiO_2 Surface Models: Energetics of the Dehydroxylation Process, Strain, *Ab Initio* Atomistic Thermodynamics and IR Spectroscopic Signatures, *Phys. Chem. Chem. Phys.*, 2016, **18**, 7475–7482.
43 P. Giannozzi, S. Baroni, N. Bonini, M. Calandra, R. Car, C. Cavazzoni, D. Ceresoli, G. L. Chiarotti, M. Cococcioni, I. Dabo, *et al.*, Quantum Espresso: A Modular and Open-Source Software Project for Quantum Simulations of Materials, *J. Phys.: Condens. Matter*, 2009, **21**, 395502.
44 P. Giannozzi, O. Andreussi, T. Brumme, O. Bunau, M. B. Nardelli, M. Calandra, R. Car, C. Cavazzoni, D. Ceresoli, M. Cococcioni, *et al.*, Advanced Capabilities for Materials Modelling with Quantum Espresso, *J. Phys.: Condens. Matter*, 2017, **29**, 465901.
45 J. P. Perdew, K. Burke and M. Ernzerhof, Generalized Gradient Approximation Made Simple, *Phys. Rev. Lett.*, 1996, **77**, 3865–3868.
46 P. Gianluca, M. Antimo, C. E. Ivano, M. Nicolas, P. Elsa and M. Nichola, A Standard Solid State Pseudopotential (SSSP) Library Optimized for Precision and Efficiency, **https://www.materialscloud.org/discover/sssp/table/efficiency**.
47 C. J. Pickard and F. Mauri, All-Electron Magnetic Response with Pseudopotentials: NMR Chemical Shifts, *Phys. Rev. B: Condens. Matter Mater. Phys.*, 2001, **63**, 245101.
48 D. Ceresoli, Pseudopotentials, **https://sites.google.com/site/dceresoli/pseudopotentials**.
49 H. J. Monkhorst and J. D. Pack, Special Points for Brillouin-Zone Integrations, *Phys. Rev. B: Solid State*, 1976, **13**, 5188–5192.
50 G. Kresse and J. Furthmuller, Efficient Iterative Schemes for Ab Initio Total-Energy Calculations Using a Plane-Wave Basis Set, *Phys. Rev. B: Condens. Matter Mater. Phys.*, 1996, **54**, 11169–11186.
51 G. Kresse and J. Furthmuller, Efficiency of *Ab initio* Total Energy Calculations for Metals and Semiconductors Using a Plane-Wave Basis Set, *Comput. Mater. Sci.*, 1996, **6**, 15–50.
52 L. F. Zhang, J. Q. Han, H. Wang, R. Car and E. Weinan, Deep Potential Molecular Dynamics: A Scalable Model with the Accuracy of Quantum Mechanics, *Phys. Rev. Lett.*, 2018, **120**, 143001.
53 D. J. Liu and J. W. Evans, Fluorine Spillover for Ceria- vs Silica-Supported Palladium Nanoparticles: A MD Study Using Machine Learning Potentials, *J. Chem. Phys.*, 2023, **159**, 024101.
54 A. H. Larsen, J. J. Mortensen, J. Blomqvist, I. E. Castelli, R. Christensen, M. Dulak, J. Friis, M. N. Groves, B. Hammer, C. Hargus, *et al.*, The Atomic Simulation Environment-A Python Library for Working with Atoms, *J. Phys.: Condens. Matter*, 2017, **29**, 273002.